Volume 419, 15 April 2022

ISSN 0096-3003

ELSEVIER

# Applied Mathematics and Computation

# Applied Mathematics and Computation

**COUNTRY**

United States

Universities and research institutions in United States

**SUBJECT AREA AND CATEGORY**

Mathematics
Applied Mathematics
Computational Mathematics

**PUBLISHER**

Elsevier Inc.

**H-INDEX**

145

**PUBLICATION TYPE**

Journals

**ISSN**

00963003, 18735649

**COVERAGE**

1975-2021

**INFORMATION**

Homepage

How to publish in this journal

amc.journal@elsevier.com

**SCOPE**

Applied Mathematics and Computation addresses work at the interface between applied mathematics, numerical computation, and applications of systems – oriented ideas to the physical, biological, social, and behavioral sciences, and emphasizes papers of a computational nature focusing on new algorithms, their analysis and numerical results. In addition to presenting research papers, Applied Mathematics and Computation publishes review articles and single–topics issues.



Quartiles

**FIND SIMILAR JOURNALS**

1
**Computational and Applied Mathematics**
USA
**70%**
similarity

2
**Journal of Applied Mathematics and Computing**
DEU
**65%**
similarity

3
**Mathematical Modelling and Analysis**
LTU
**65%**
similarity

4
**International Jou Applied and Com**
IND
**64**
simila

SJR

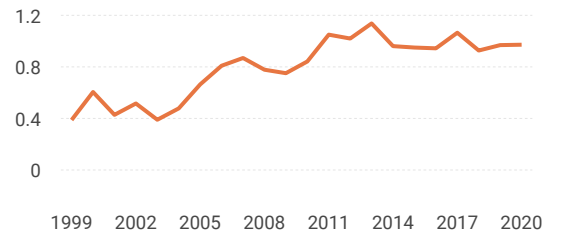


Total Documents

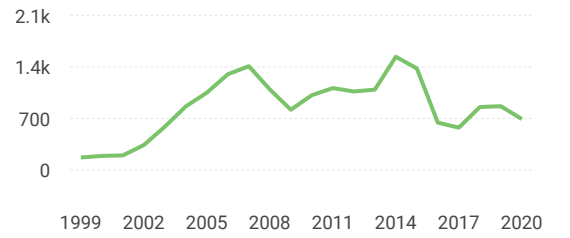


Total Cites Self-Cites

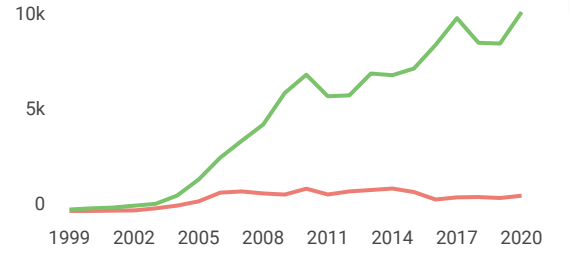


External Cites per Doc Cites per Doc

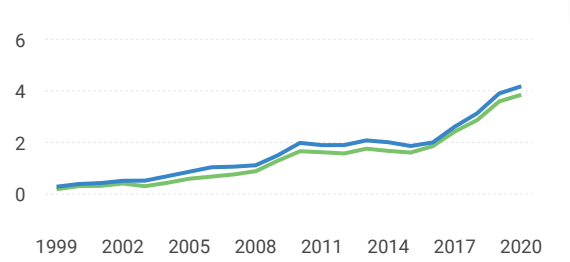


Citations per document

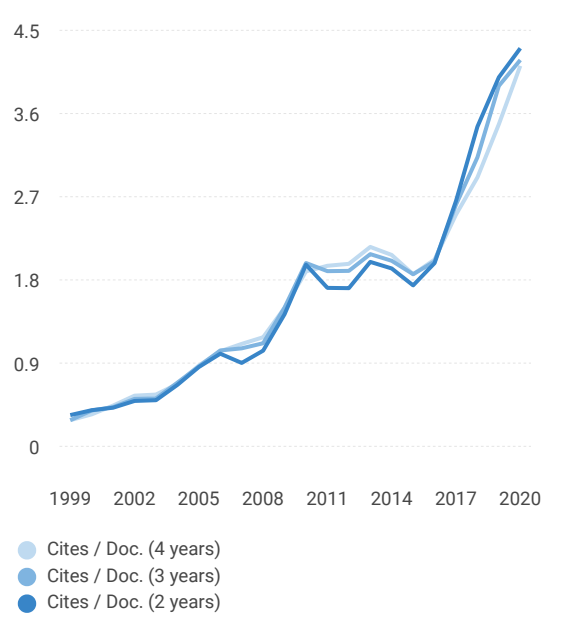


% International Collaboration

Citable documents Non-citable documents

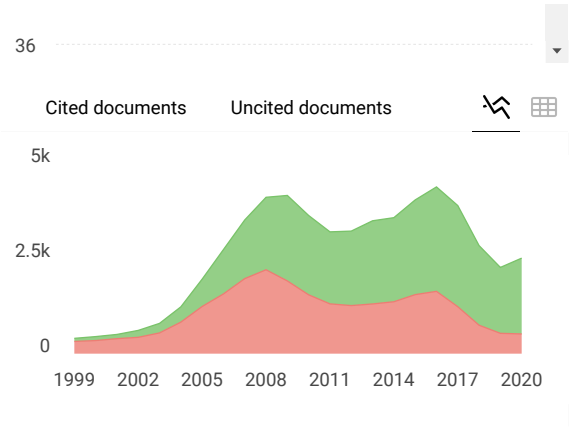


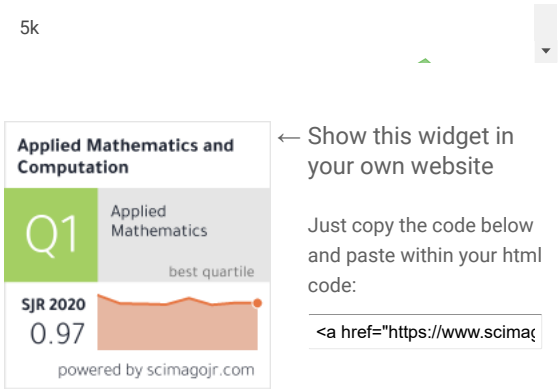




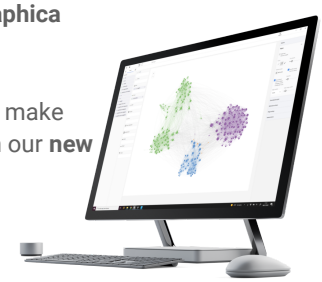

Metrics based on Scopus® data as of April 2021

M **Maedeh** 1 year ago

hi

reply

SCImago Team

**Melanie Ortiz** 1 year ago

Dear Maedeh, welcome and thanks for your participation! Best Regards, SCImago Team

**Leave a comment**

Name

Email
(will not be published)

The users of Scimago Journal & Country Rank have the possibility to dialogue through comments linked to a specific journal. The purpose is to have a forum in which general doubts about the processes of publication in the journal, experiences and other issues derived from the publication of papers are resolved. For topics on particular articles, maintain the dialogue through the usual channels with your editor.

Applied Mathematics and Computation 411 (2021) 126490

Contents lists available at ScienceDirect

Applied Mathematics and Computation

journal homepage: www.elsevier.com/locate/amc

# Investigating the effects of viscosity and density ratio on the numerical analysis of Rayleigh-Taylor instability in two-phase flow using Lattice Boltzmann method: From early stage to equilibrium state

Bahrul Jalaali[a], Muhammad Ridlo Erdata Nasution[b], Kumara Ari Yuana[c], Deendarlianto[d,e], Okto Dinaryanto[a,*]

[a] Department of Mechanical Engineering, Faculty of Aerospace Technology, Institut Teknologi Dirgantara Adisutjipto, Blok R Lanud Adisutjipto, Yogyakarta 55198, Indonesia
[b] Department of Aerospace Engineering, Faculty of Aerospace Technology, Institut Teknologi Dirgantara Adisutjipto, Blok R Lanud Adisutjipto, Yogyakarta 55198, Indonesia
[c] Department of Informatics, Faculty of Computer Science, Universitas Amikom Yogyakarta Jl Ringroad Utara, Yogyakarta 55281, Indonesia
[d] Department of Mechanical and Industrial Engineering, Faculty of Engineering, Universitas Gadjah Mada, Jalan Grafika 2, Yogyakarta 55281, Indonesia
[e] Center for Energy Studies, Universitas Gadjah Mada, Sekip K-1A Kampus UGM, Yogyakarta 55281, Indonesia

ARTICLE INFO

*Article history:*
Received 25 June 2020
Revised 23 June 2021
Accepted 28 June 2021

*Keywords:*
Liquid-liquid two-phase flow
Rayleigh-Taylor instability
Lattice-Boltzmann method
Viscosity
Density ratio

ABSTRACT

The gravitational liquid-liquid two-phase flow was numerically investigated by using lattice Boltzmann method (LBM). The method was implemented for analyzing a model of Rayleigh-Taylor Instability (RTI). The feasibility of this present numerical approach was investigated by performing convergence test, and validating the obtained results with those obtained from experiments as well as other preceding numerical methods. Qualitative and quantitative comparisons were examined, whereby good agreements are noted for all cases. Parametric studies were also conducted by varying both of Reynolds and Atwood numbers to investigate the effects of viscosity and density ratio on the behavior of fluids interaction. Based on the obtained outcomes of this numerical approach, the present LBM was able to successfully simulate the complete phenomena during RTI, i.e.: the linear growth, secondary instability, bubble rising and coalescence, and liquid break-up, including turbulent mixing conditions as well as the equilibrium state. The finding obtained from this work might be beneficial in the investigation of parametric behavior in design of processes equipment such as for separator design.



## 1. Introduction

The liquid-liquid two-phase flow is often encountered in many applications within petroleum industries [1–3], e.g.: oil-water separation process [4, 5]. The gravitational liquid-liquid two-phase flow has been becoming the object of multiphase studies and is related to the demand of oil process operation [6–8]. Flow instabilities were frequently found in the liquid-

* Corresponding author at: Department of Mechanical Engineering, Faculty of Aerospace Technology, Institut Teknologi Dirgantara Adisutjipto.
*E-mail address:* okto.dinaryanto@mail.ugm.ac.id (O. Dinaryanto).

https://doi.org/10.1016/j.amc.2021.126490
0096-3003/

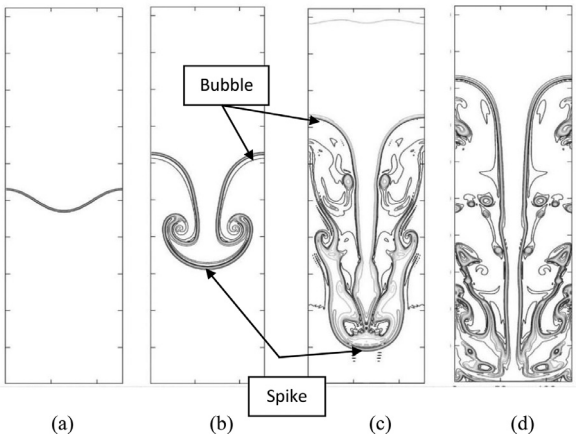


**Fig. 1.** The growth of RTI phenomena: (a) first stage, (b) second stage, (c) third stage, and (d) fourth stage.

liquid two-phase flow [2], for instance, fluid mixing and separation in gravity separator devices [8]. The operation of gravity separator plays an important role for separating fluid phases before transporting into facilities [9]. In the design development of fluid separation equipment, cost reduction becomes one of major concerns. This can be achieved by minimizing the space and weight of equipment, as well as accelerating the separation process [3]. Several complexities are particularly found in the design of separator, such as the consideration of residence and surge times which relates to fluid's equilibrium state and its performance [7, 10], whereas those parameters are influenced by physical properties such as viscosity and density [10, 11] and the rate of achieving the equilibrium state is presented as the instability rate [12–14]. Hence, it is important to improve the understanding of instability behavior of fluid interaction in the design consideration of separator.

The gravity separator involves a phenomenon whereby the denser fluid flows downward through the lighter fluid due to the body force of gravity [12, 13, 15, 16]. The presence of body force in stratified multiphase flow with zero velocity gradient emergences the buoyancy-driven instability called Rayleigh-Taylor Instability (RTI). The RTI occurs when two fluids with different density have an opposing trend between pressure and density gradients [15]. It leads to a regime of turbulent or chaotic mixing of two fluids. The mixing is attained after several stages as follows: (i) initial perturbation wave growth (Fig. 1(a)); (ii) the movement of heavier fluid into the lighter fluid in the form of round-topped bubbles due to their different densities (Fig. 1(b)); (iii) the development of spikes and Helmholtz instability phenomenon (Fig. 1(c)); (iv) the forming of turbulent regime (Fig. 1(d)) [17–20]. The presence of turbulent mixing generates vibration effects [17, 21], such as resonance, which may lead to significant damage to the device [1]. Consequently, the aforementioned phenomena should be considered in the design of gravity separator. The flow instability behavior is important to be comprehensively investigated from its initial state to the complete equilibrium state (i.e. the complete separation between two fluids). Whereas the depth understanding of instability behavior in design consideration of oil-gas devices is indispensable since instability is an unpredicted phenomenon. However, to the best of authors' knowledge, there exist only a few researches involving the equilibrium state of RTI.

Several previous works had been analytically carried out by using linear stability theory [15]. However, some employed assumptions yielded inaccurate results. Waddell et al. [22] experimentally investigated RTI by varying the density ratio using a heptane-water mixture. In the early stages, spikes and bubbles were formed and the instability rate was growing exponentially. Meanwhile, the instability rate in the late stages can be considered to increase linearly. In this regard, the similar trends were particularly found at low Reynold number in the research of Lewis [23] and Wilkinson et al. [24]. The experimental results clarified that the analytical solution was only valid for the early stages of RTI. The analytical solution started to deviate at the late stages of RTI since the forming of the turbulent mixing regime. The flow behavior in the turbulent mixing depended on the fluid properties, i.e.: viscosity and density ratio, numerically represented by Reynolds and Atwood numbers, respectively. Both properties were also found to affect the instability rate [22, 24–26]. Thus, RTI behavior needs to be carefully investigated by means of varying the value of Reynolds and Atwood numbers. However, this would be quite cumbersome to do in experiments.

The investigation of material properties and behavior including instability phenomenon can be efficiently performed through the use of numerical analysis [1, 27]. In RTI, numerical analysis is often performed by either conventional mesh or mesh-less methods [16, 17, 28, 48, 49]. Numerous numerical methods had been able to successfully simulate the initial stages of RTI, for instance, the phase-field method [21], finite element approach [29], radial basis function [30] and vortex in cell [31]. Nevertheless, those studies were still not able to simulate RTI in the equilibrium state, while numerical instability was still found when solving a complex governing equation. Lee et al. [21] used phase-field method and successfully generated the RTI to an equilibrium state. On the other hand, it lacked a clear physical explanation.

The particle-based method that has been developed into a powerful and efficient method for an immense range of fluid cases is Lattice Boltzmann Method (LBM) [32–34]. LBM has advantages in completely linear of convective operator

(streaming process) than non-linear Navier-Stokes equations, which makes it less difficult to solve. Furthermore, LBM utilizes the equation of states, and this yields that Poisson equation is not necessarily to be solved in order to obtain pressure terms. LBM is able to formulate the simple mechanical rules for declaring the complex boundary condition [34–36]. Several LBM methods had been developed to approximate multiphase flow cases. Gunstensen et al. proposed color-gradient LBM [37]. In the study, inaccurate results of multiphase flow were obtained. The free-energy LBM was proposed by Swift et al. [38] by utilizing more complex equation and lack of Galilean invariance which was numerically inefficient. Further, both color-gradient and free-energy methods need to be numerically improved [34, 39]. The pseudopotential method was developed by Shan-Chen (SC). The method possessed several advantages in both numerical efficiency and simpler governing equation. Yet, thermodynamics consistency, numerical accuracy, and limited Reynolds number become the weakness of this method [34, 39–40]. He et al. [17] introduced the novel LBM (HCZ) to overcome the limitation of the SC method. The method utilized an index function to define a fluid interface. Furthermore, HCZ is able to facilitate a higher density ratio and Reynolds number [41]. Cited from Huang et al. [42], HCZ model can be improved by modifying the force scheme into that of Chao et al. [43]. The LBM for RTI cases had been previously employed by Fakhari et al. [44]. The study was able to simulate RTI at high Reynolds and Atwood numbers. However, the investigation of equilibrium state was not performed. The implementation of the forcing scheme is used in this study to analyze the behavior RTI and became the distinguish and improvisation aspect compared with the related-previous studies.

The aim of this paper is to conduct the physical phenomena analysis of RTI from early stage to equilibrium state by using unconventional numerical method of fluid. The analysis employs a novel perspective in comparison with previous studies for a model of immiscible liquid-liquid two-phase flow in accordance with practical case. Assessments of the impact of viscosity and density ratio to the fluid instability is performed whereby viscosity is represented as Reynolds while that of density ratio is related to Atwood numbers. In this paper, RTI simulation is carried out until the RTI late-stage or after the emerged of secondary instability using modified-LBM. The RTI in the turbulent mixing regime consists of several fluid phenomena such as bubble and spike coalescence, emerging of secondary instability and liquid break-up. This paper also aims to enrich the study of late-stage instability behavior in liquid-liquid two-phase numerical model, which is, to the best of authors' knowledge, not easily found in the current literature. In order to examine the plausibility of the proposed approach, the results of present analysis are compared to those of other conventional mesh method as well as mess-less method.

## 2. Methods

The observation domain of LBM is a mesoscopic scale that considers a set of particles as a unit without considering the behavior of each particle [32]. In order to determine the property of the set of particles, a distribution function is introduced. The function is defined as a statistical description of a system that characterizes the properties of particles. By applying the law of similarity, dimensionless parameters can be used to link between the properties in mesoscopic and macroscopic domains [32, 33].

In the present analysis, a discrete distribution function is employed for simulating liquid-liquid flow. The simulation adopts the HCZ model, which is linked to the authors' previous work of Kumara et al. [48]. It has a limitation that the density ratio between both fluids should be more than 0.1 [42]. In the case of the investigation of two phases with high-density ratio, such as liquid-gas flow, extension analyses employing LBM can be found in the researches of Fakhari et al. [44] and Geier et al. [50]. It is also worthwhile to consider several numerical analyses in the framework of finite element method in Refs. [51,52].

In this proposed method, the analysis of liquid-liquid two phase flow utilizes two distribution functions namely index distribution function and pressure distribution function as expressed in Eqs. (1) and 2, respectively. The index distribution function performs as a tracking interface, while pressure distribution function is beneficial to analyze the physical properties. Two source terms (i.e. $Sf_i(\boldsymbol{x},t)$ and $Sg_i(\boldsymbol{x},t)$) are included in the distribution functions. Both terms are defined in Eqs. (3) and 4. In those equations, the term $\Gamma_i(\boldsymbol{u})$ is described as $\frac{f_i^{eq}}{\phi}$, whereby $\varphi$ denotes index function (Eq. (5)). The index functions have to be explicitly defined to distinguish between the value of each fluid phase. The value of $\varphi_h$ and $\varphi_l$ can be theoretically obtained by Maxwell construction. The value of $\varphi_h$ and $\varphi_l$ are shown as follows:

$$\phi = \begin{cases} fluid\ 1, & \phi_h \\ interfacial\ region, & \phi_h < \phi < \phi_l \\ fluid\ 2, & \phi_l \end{cases}$$

The function of $\psi(\varphi)$, included in Eq. (3), is necessary in two-phase flow simulations to imitate the physical intermolecular interaction in terms of particle collisions. In fluids problem, the particle collisions are influenced by surface tension $F_s$ and effective force $\psi(\rho)$.

$$f_i(\boldsymbol{x}+\boldsymbol{e}_i\delta_t, t+\delta_t) - f_i(\boldsymbol{x},t) = -\frac{\left(f_i(\boldsymbol{x},t) - f_i^{eq}(\boldsymbol{x},t)\right)}{\tau_f} + Sf_i(\boldsymbol{x},t)\delta_t \tag{1}$$

$$g_i(\boldsymbol{x}+\boldsymbol{e}_i\delta_t, t+\delta_t) - g_i(\boldsymbol{x},t) = -\frac{(g_i(\boldsymbol{x},t) - g_i^{eq}(\boldsymbol{x},t))}{\tau_g} + Sg_i(\boldsymbol{x},t)\delta_t \tag{2}$$

$$S_f(\boldsymbol{x},t) = -\Gamma_i(\boldsymbol{u})\frac{2\tau_f - 1}{2\tau_f}\frac{(\boldsymbol{e}_i - \boldsymbol{u}).\nabla\psi(\phi)}{RT} \tag{3}$$

$$S_g(\boldsymbol{x},t) = -\frac{2\tau_g - 1}{2\tau_g}(\boldsymbol{e}_i - \boldsymbol{u}).[\Gamma_i(\boldsymbol{u}).(F_s + G) - (\Gamma_i(\boldsymbol{u}) - \Gamma_i(0))\nabla\psi(\rho)] \tag{4}$$

$$\phi = \sum f_i \tag{5}$$

$$\rho(\phi) = 1 + \frac{\phi - \phi_l}{\phi_h - \phi_l}\left(\frac{\rho_1}{\rho_2} - 1\right) \tag{6}$$

$$\nu(\phi) = 1 + \frac{\phi - \phi_l}{\phi_h - \phi_l}\left(\frac{\nu_1}{\nu_2} - 1\right) \tag{7}$$

$$p = \sum g_i - \frac{\boldsymbol{u}}{2}.\nabla\psi(\rho)\delta_t \tag{8}$$

$$\boldsymbol{u} = \frac{\left(\sum \boldsymbol{e}_i g_i + \frac{RT}{2}(\boldsymbol{F}_s + \boldsymbol{G})\delta_t\right)}{\rho RT} \tag{9}$$

In Eq. (4), the multiplication of a considerably small term $(\Gamma_i(u) - \Gamma_i(0))$ and effective force $\nabla\psi(\rho)$ is done in order to reduce numerical error [43]. It is noted that $\Gamma_i(u) - \Gamma_i(0)$ is comparable to the Mach number in weakly incompressible limit. The density and kinematic viscosity are expressed in Eqs. (6) and 7, as a function of $\varphi$. In both equations, the densities $\rho_1$and $\rho_2$ are those of fluids with higher and lower density value, respectively. The pressure distribution function $(g_i)$ is then utilized to calculate pressure and macroscopic velocity as defined in Eqs. (8) and 9.

The distribution functions in equilibrium condition are shown in Eqs. (10) and 11. Here, the functions are obtained by setting the relaxation time $\tau_f$ and $\tau_g$ to be equal. The relaxation time $\tau$ is linked to the kinematic viscosity which is defined as $\upsilon = \frac{c^2}{3}(\tau - \frac{1}{2})\delta_t$. It is noteworthy that, in Eq. (10), $c = \sqrt{RT}$. The terms of $R$, $T$ and $w_i$ are the gas constant, temperature, and weighting factors, respectively.

$$f_i^{eq}(\boldsymbol{x},t) = w_i\phi\left[1 + \frac{3\boldsymbol{e}_i.\boldsymbol{u}}{c^2} + \frac{9(\boldsymbol{e}_i.\boldsymbol{u})^2}{2c^4} - \frac{3\boldsymbol{u}^2}{2c^2}\right] \tag{10}$$

$$g_i^{eq}(\boldsymbol{x},t) = w_i\left[p + \rho RT\left(\frac{3\boldsymbol{e}_i.\boldsymbol{u}}{RTc^2} + \frac{9(\boldsymbol{e}_i.\boldsymbol{u})^2}{2RTc^4} - \frac{3\boldsymbol{u}^2}{2RTc^2}\right)\right] \tag{11}$$

$$\boldsymbol{F} = \boldsymbol{F}_s + \boldsymbol{G} = \kappa\rho\nabla\nabla^2\phi + g.\rho \tag{12}$$

In this study, the external and body forces are considered through the use of gravity force $(G)$ and surface tension $(F_s)$. The sum of total forces is given in Eq. (12). The term $\kappa$ relates the magnitude of surface tension. Numerical model is observed in two-dimensional space with nine directions of motion (D2Q9). The weighting factor of the configuration is expressed as:

$$w_i = \left\{\begin{array}{lll}(4/9) & , & i = 0\\ (1/9) & , & i = 1,2,3,4\\ (1/36) & , & i = 5,6,7,8\end{array}\right\}$$

The corresponding discrete velocities $(\boldsymbol{e_i})$ for each direction can be defined as follows:

$$e_i = \left\{\begin{array}{ll}(0,0), & i = 1\\ (sin\alpha_i, cos\alpha_i), & i = 2,\ 4,\ 6,\ 8;\quad \alpha_i = \left(\pi - \frac{\pi i}{4}\right)\\ \sqrt{2}(sin\alpha_i, cos\alpha_i), & i = 3,\ 5,\ 7,\ 9\end{array}\right\}$$

The numerical model utilized in this numerical works is shown in Fig. 2. In this figure, $v_x$ and $v_y$ denote the velocity components, $L$ and $H$ respectively indicate the domain length and height, $g$ is the gravitational force, while $f_a, f_b, g_a$ and $g_b$ are the distribution functions.

A perturbation wave is subjected to the interface between two fluids. The wave is expressed in Eq. (13), whereby $A$ is the wave amplitude and $n$ denotes the wavelength. A small initial perturbation wave $(y)$ is also given by Eq. (13) as an initial condition where $x$ and $n$ is the length and number of wave, respectively. In the model, bounce-back boundary conditions are applied at the top and bottom walls. The right and left sides of the model are under periodic boundary conditions (Eq. (14))

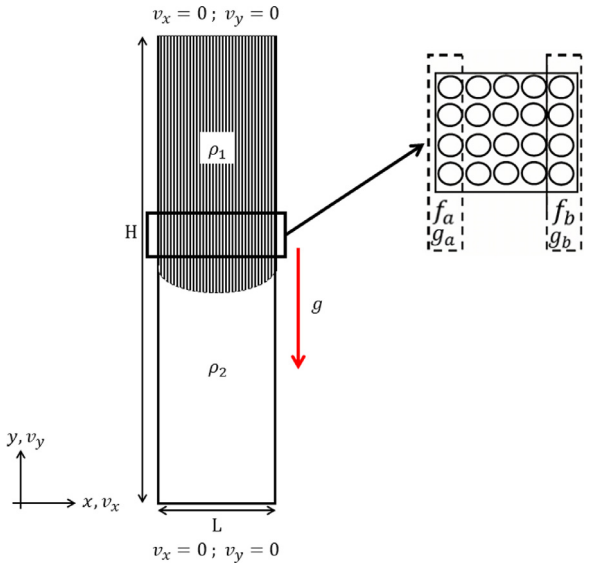


**Fig. 2.** Numerical model of RTI simulation.

illustrated in Fig. 2. Furthermore, gravity force is applied in the fluid interface as well.

$$y = \frac{H}{2} + 0.1An\ cos\left(\frac{2\pi x}{n}\right) \tag{13}$$

$$f_a = f_b; g_a = g_b \tag{14}$$

The simulation results are presented in dimensionless quantities. The utilized dimensionless parameters are timestep ($ts$), Reynolds number ($Re$), and Atwood number ($A_t$). The Reynolds number is the ratio between inertia and viscous forces. It is expressed by $Re = \frac{L\sqrt{L\ g}}{\nu}$. Meanwhile, the Atwood number which related to the density ratio between both fluids can be defined as $A_t = \frac{\rho_1 - \rho_2}{\rho_1 + \rho_2}$. The time domain is characterized using timesteps ($ts$) expressed as $T = \sqrt{\frac{L}{g}}$.

## 3. Results and discussion

In the present study, the observation domain is shown in Fig. 3. In this figure, schematic representation of spike and bubble with respect to the position is given. The analysis will evaluate the height of the bubble ($h_b$) and spike ($h_b$) amplitude at certain timesteps.

A grid independence test was firstly conducted. The test was carried out by varying the number of lattices while keeping the physical parameters at constant values. This test aims to provide the value of independence lattices where the calculations start to obtain convergent results. The test utilizes two cases with different Reynolds number (i.e. $Re = 256$ and $Re = 1024$). Meanwhile, the total number of lattices are varied as follows: 25,600; 40,000; 65,536; 90,000; and 122,500. The simulations were carried out by using geometry with aspect ratio of 1:4 for $L$ and $H$ values. The results are given in Fig. 4, whereby only a small change of the spike amplitude exists in the results of both $Re = 256$ and $Re = 1024$ for lattice number of 65,536 and above. Meanwhile, the numerical time tends to increase exponentially as the increase of lattices number as clearly shown in Fig. 5. The aforementioned facts conclude that the number of lattices of 65,536 can be regarded as the optimum value in this analysis, and will be used for the rest calculation.

In this paper, the validations are performed by comparing the results obtained from the current analysis with those of other numerical methods [21, 31, 44–46] as well as available experiment data [22, 24] from open literature. The spikes and bubble positions are considered as quantitative parameters. Numerical validations were conducted by simulating the RTI model under the flow condition of $Re = 3000$ and $A_t = 0.5$. Both LBM-based and non-LBM methods are utilized as comparing methods. In this study, the non-LBM methods used for comparison purpose are Vortex in cell method [31] and finite difference-phase field meshless method [20]. The validation results are shown in Fig. 6.

In the case of validation with the experimental study [22], a numerical model with physical parameters of $A_t = 0.156$ and $Re = 6000$ is employed. Besides, the experimental study conducted by Wilkinson covers the early stages of RTI with $A_t = 0.15$ [24]. The numerical and experimental results are quantitatively and qualitatively compared. Here, the magnitude of bubble amplitude is quantitatively studied in terms of spike and bubble position. Fig. 7a shows the comparison of bubble and spike position between numerical and experimental results. From this figure, at T of about 0.2 s, the deviation between both results tends to increase. This phenomenon occurs due to the fluids turbulence mixing condition. However, within

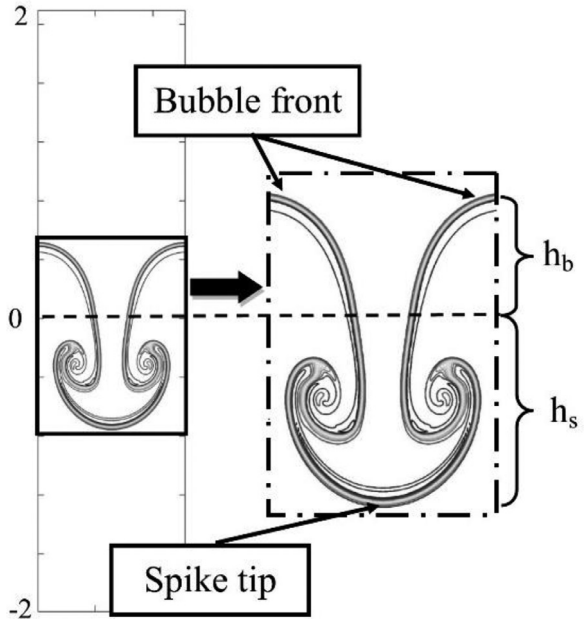


**Fig. 3.** Schematic definition of bubble ($h_b$) and spike ($h_s$) amplitude.

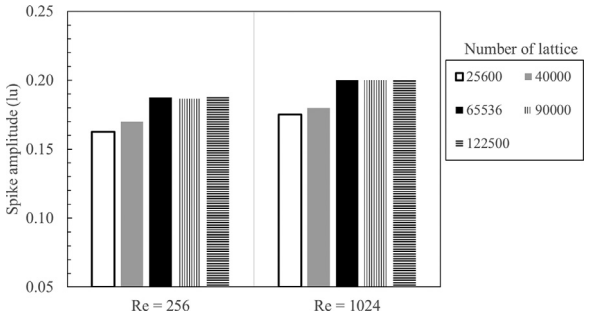


**Fig. 4.** The value of spike amplitude for varied number of lattice at particular Reynolds number.

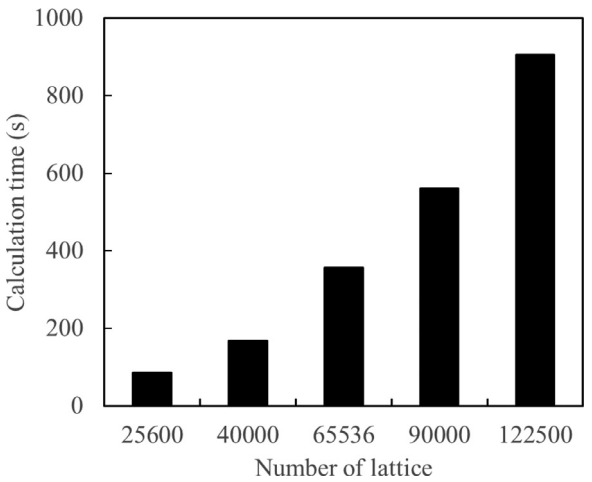


**Fig. 5.** The duration of simulation at certain number of lattice.

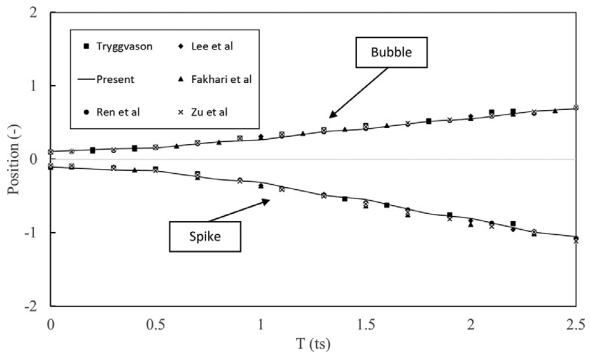


**Fig. 6.** Simulation results for bubble and spike position of current model compared with others numerical study.

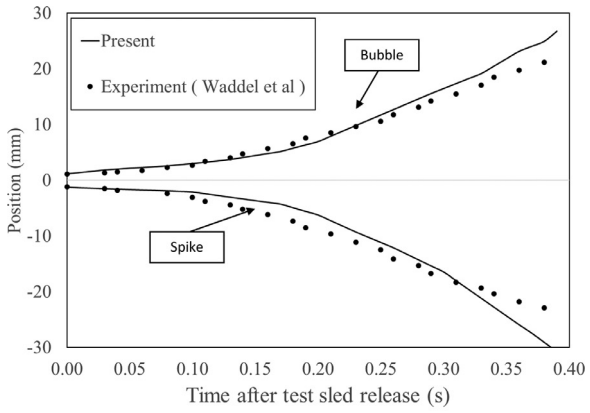


A)

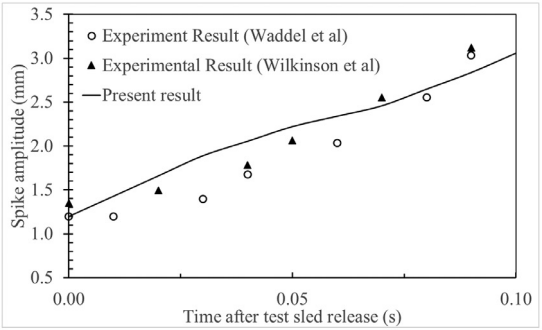


b)

**Fig. 7.** a) The spike and bubble position of simulation and experimental of Ref. [22] result comparison. b) The amplitude of bubble comparison in early stages RTI.

the early stage ($T = 0$ to 0.2), both simulation and experimental values are in good agreements. Fig. 7b shows the bubble amplitude of present study compared with those of Refs. [22] and [24]. Good agreements are also observed during the early stage of RTI. Furthermore, the qualitative comparison results are shown in Fig. 8. In this figure, the visual representation of early stage RTI is successfully simulated. This fact can be exhibited by a similar pattern of spikes and bubbles between simulation and experimental results for several certain time.

For sake of accuracy assessment of the simulation, mean absolute percentage error (*MAPE*) is calculated by the following equation:

$$MAPE = \frac{1}{n}\sum_{i=1}^{n}\left|\frac{X_{s,i} - X_{c,i}}{X_{c,i}}\right| x100\% \tag{14a}$$

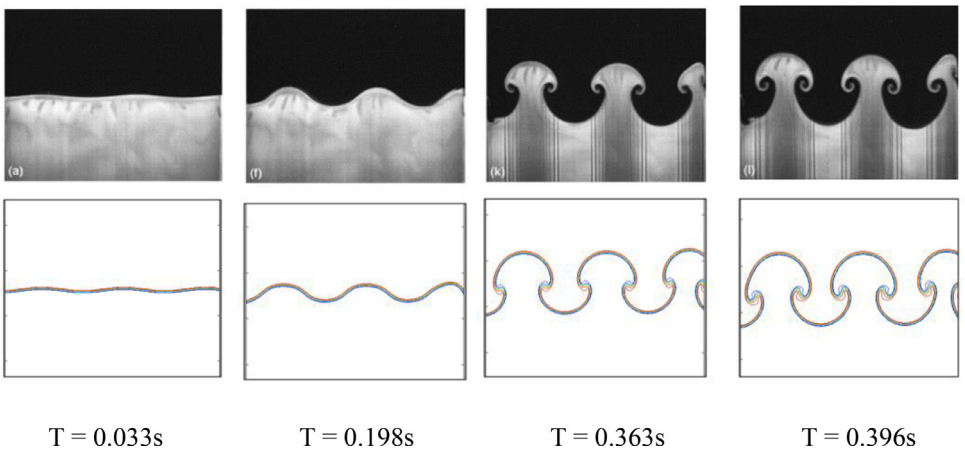


**Fig. 8.** Comparison of numerical (below) and experimental (above) result of Waddell et al. [22] at certain time.

**Table 1**
MAPE value of numerical and experiment benchmarking.

| MAPE of position comparison with present result | | | |
|---|---|---|---|
| | Bubble | Spike | Total MAPE value |
| **Numerical Studies** | | | |
| Tryggvason [31] | 7.17% | 8.66% | 7.85% |
| Lee et al. [20] | 8.10% | 5.28% | 6.49% |
| Fakhari et al. [44] | 4.12% | 8.21% | 5.72% |
| Zu et al. [45] | 5.39% | 9.43% | 7.34% |
| Ren et al. [46] | 3.72% | 8.93% | 6.32% |
| **Experimental Study** | | | |
| Waddel et al. [22] | 12.72% | 25.62% | 19.03% |

In Eq. (14), $X_{s,i}$ is the result of present analysis while $X_{c,i}$ denotes the result of comparative study. The calculated *MAPE* values are shown in Table 1. The results reveal that the obtained *MAPE* value for bubble position between simulation and experiment is 12.72% while those between the present simulation and other numerical analyses are less than 10%. In terms of spike position, *MAPE* value between simulation and experiment is 25.62% which is still considered as a reasonable accurate. Meanwhile, *MAPE* value for spike position is not more than 10% as compared to other numerical studies. This fact yields that the current LBM analysis is able to accurately simulate the liquid-liquid two-phase of RTI problem.

In order to investigate the effects of viscosity and density ratio on RTI behavior, parametric studies varying several sets of Reynolds and Atwood numbers are performed. In the parametric study of *Re*, three different Reynolds numbers were varied (i.e. $Re = 256; 512; 1024$) under a constant $A_t = 0.5$. Meanwhile, variations of Atwood numbers of 0.1, 0.3, and 0.5 are also utilized in the parametric study of $A_t$ under a constant of $Re = 1024$. Here, the instability rate will be investigated by considering the spike and bubble position. In terms of separator design, instability rate is closely related to the surge and residence time in fluid separation process. The RTI stages are shown in Fig. 9.

The results of parametric study of the effect of *Re* are shown in Figs. 10 and 11 for the bubble and spike positions, respectively. In general, spikes and bubble positions tend to be quickly shifted for $Re = 1024$ than $Re = 512$ and 256. The lower *Re* means the higher viscous force, consequently, the bubble and spike traveled-distance will be slightly delayed compared to a higher *Re* due to the ability to hold the gravitational force up. In the figures, the discrepancies of both spikes and bubble positions between the results of $Re = 1024$ and 512 with respect to $Re = 256$ are given. At $T < 1$, the spikes and the bubbles are shifted constantly experiencing the linear growth instability. Meanwhile, the fluid roll-up emerges as a result of shear force as shown in $T = 3$ for $Re = 1024$. Although the spike position is slightly the same, the fluids roll-up for $Re = 1024$ is firstly formed than others. The higher *Re* leads the fluid to become less viscous, hence the fluids frictional force decreases. The rolling-up fluid exhibits the secondary instability of Kelvin-Helmholtz instability (KHI). The spike displacement is slightly delayed during the rolling up process. This phenomenon occurs due to the interaction between gravitational and viscous forces on the fluid interface. Furthermore, the emergence of KHI causes spike to be accelerated at $T = 4$. Meanwhile, for smaller *Re*, the instability rate was low and the effect of KHI was suppressed due to the less deformable behavior of fluid. A deeper investigation of spike position results in a tendency of spike to fall slightly faster in higher *Re*. At $Re = 1024$, the stages of instability are clearly observed (i.e. fluid roll-up) in comparison to the cases with lower *Re* and this trend is in line with Ref. [28].

From the above analysis, by neglecting the effect of the density ratio, viscosity (i.e. in terms of *Re*) was found to slightly influence the instability rate. However, viscosity has a significant influence in the fluid roll-up process. The vortices that

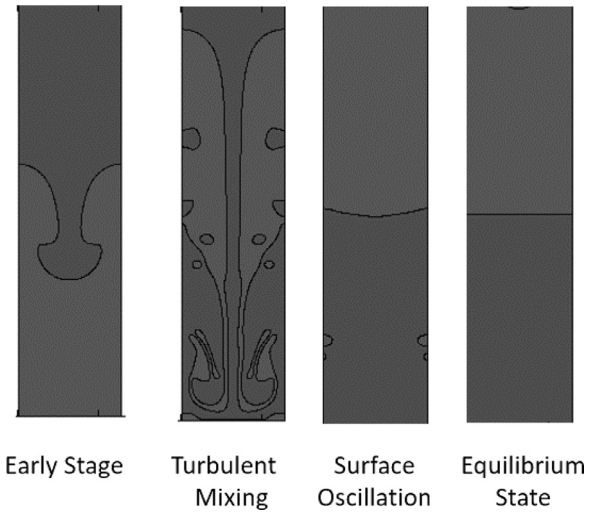


**Fig. 9.** RTI phase to equilibrium state.

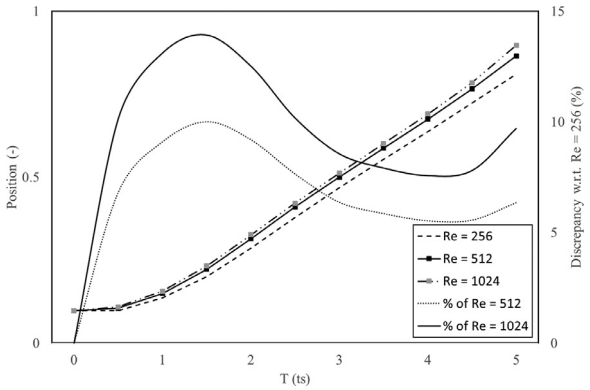


**Fig. 10.** Bubble position and value of discrepancy w.r.t $Re = 256$.

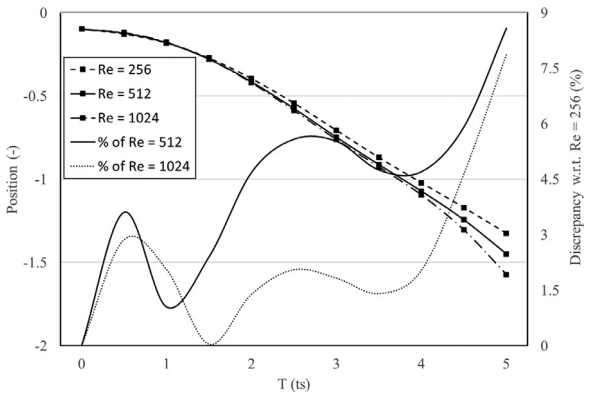


**Fig. 11.** Spike position and value of discrepancy w.r.t $Re = 256$.

occurred during the instability stages are clearly captured in the case with higher *Re*. The outcomes are in good agreement with the previous analytical study of [15, 46]. This aforementioned phenomena lead fluids to be more deformable (less viscous) and increase the duration of turbulent mixing and surface oscillation phase as shown in Figs. 12. This asserts that increasing *Re* will delay the equilibrium state, albeit it increases the instability rate.

Investigation of the effects of density ratio is performed by varying Atwood number. The results are shown in Figs. 13 and 14 for bubble and spikes, respectively. The density ratio corresponds to the effect of buoyancy force, which affects the

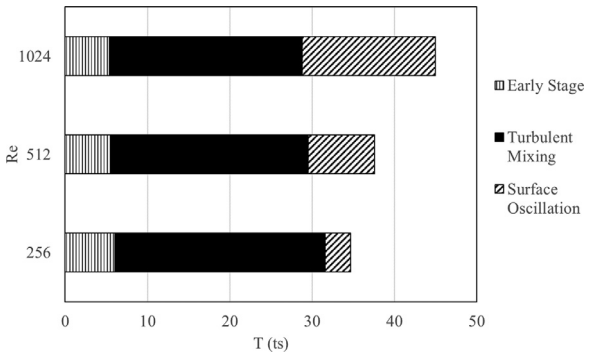


**Fig. 12.** The duration of RTI equilibrium state process for *Re* variation w.r.t. $A_t$= 0.5.

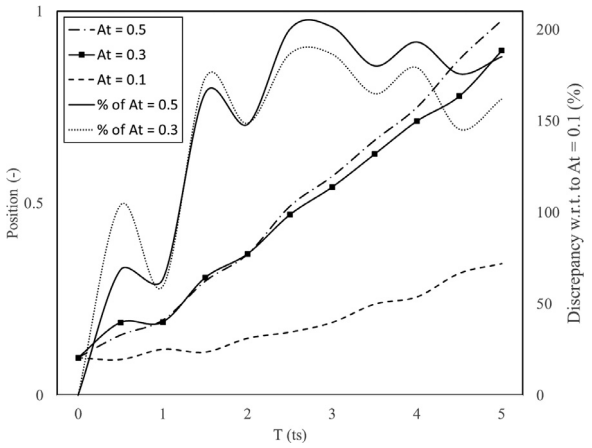


**Fig. 13.** Bubble position and value of discrepancy w.r.t. $A_t$= 0.1.

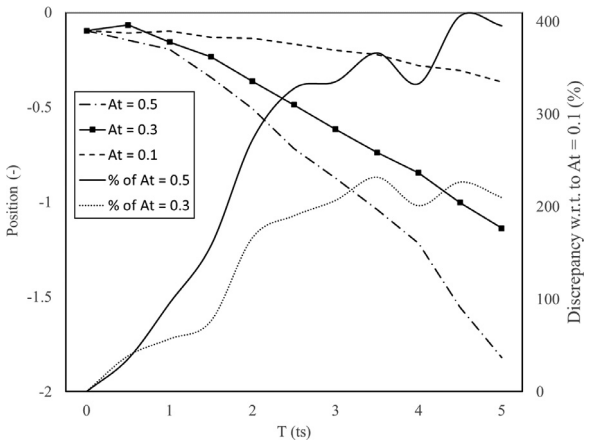


**Fig. 14.** Spike position and value of discrepancy w.r.t. $A_t$= 0.1.

lighter fluid to arise through the heavier fluid. The spike and bubble positions in the higher $A_t$ have a tendency to shift faster than lower $A_t$, therefore they are attaining to turbulent mixing phase quickly.

When T is less than 1, the bubble position of $A_t$= 0.5 is delayed due to the interaction between gravitational and viscous force at the interface. When T is more than 2, the gravitational force is dominating the viscous force, and this causes the bubble to linearly increase. The bubble positions in both $A_t$= 0.5 and 0.3 show relatively the same trend. On the other hand, at $A_t$= 0.1, the bubble position is lower because the density difference is small. Both fluids at low $A_t$are hard to be separated so that affects to the bubble and position displacement. The formation of fluid roll-up occurs at $T = 1$ for $A_t$= 0.5 and accelerates the spike position. Consequently, the spike position of $A_t$= 0.5 has a quicker decrease than that of $A_t$= 0.1 and

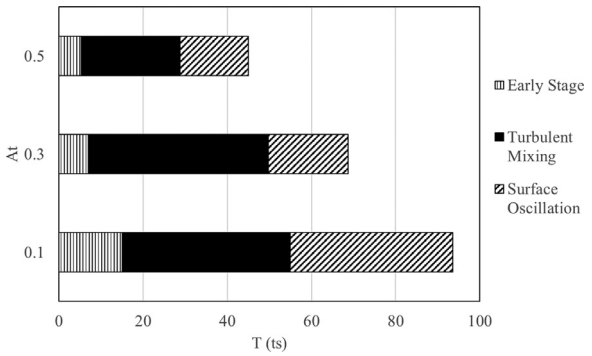


**Fig. 15.** The duration of RTI equilibrium state process for $A_t$ variation w.r.t $Re = 1024$.

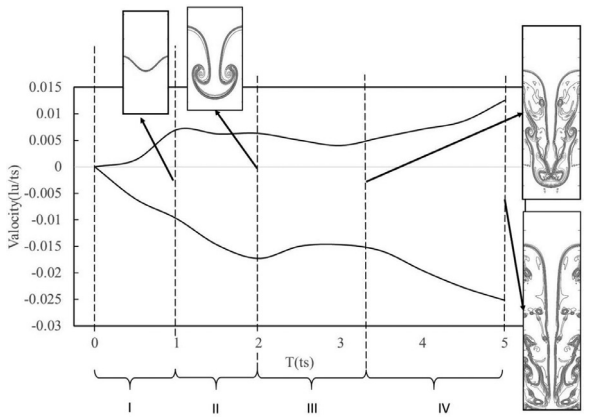


**Fig. 16.** Plot of spike and bubble velocity and the region of early stages instability.

0.3. Meanwhile, for $A_t$= 0.1, spike falls slower and smoother as the fluid roll-up is holding up, hence the spike acceleration is delayed. It may be concluded that due to the lower buoyancy force, $A_t$= 0.1, it will gradually rise than in the case with higher At. The buoyancy force causes a lighter fluid to move upwards faster than the heavier one. This may relates to the surge and residence time in separator design considerations. As shown in Fig. 15, the equilibrium state for higher $A_t$ is quickly attained than that of lower $A_t$. The higher density ratio means that the fluids are rapidly entering the turbulent mixing and equilibrium state, and consequently yields a lower surge and residence time. Contrarily, fluids with similar densities are difficult to be separated and will have higher surge and residence time. In terms of separator design, such fluid behavior should be considered in the design of separator length. The aforementioned facts show that the instability rate was strongly influenced by the density ratio. This agrees with some findings in existing analytical studies [14, 15] as well as experimental work in Ref. [26].

In comparison to the effect of *Re*, the discrepancy of both bubbles and spike positions with respect to the results obtained by the lowest value of $A_t$ (0.1) tend to be more fluctuated. From Figs. 13 and 14, it is found that the increase of $A_t$of three times (i.e. from 0.1 to 0.3) results in the maximum value of discrepancy of about 180% and 210% for bubble and spike positions, respectively. Meanwhile, in Figs. 9 and 10, the discrepancies obtained due to the increase of *Re* from 256 to 1024 (four times) are less than 15%. These facts indicate that $A_t$has more dominant effects on the traveled-distance of spike and bubbles and instability rate, as compared to *Re*. This also agrees with the findings in other available literatures in Refs. [17, 20, 46]. It can be concluded that density ratio has a more dominant role, as compared to the viscosity, in the instability rate.

In this study, RTI simulation was performed in a complete manner. The simulation covers the early stages of instability, turbulent mixing phase, as well as the equilibrium state as the last stage. Investigation of the early stages is divided into four region, as can be seen in Fig. 16. The first region exhibits that the gravitational force start to penetrate against the fluids viscous force. The gravitational force will force the denser fluid to penetrate into the lighter fluid. This causes both bubbles and spike to accelerate fast as the buoyancy force of the lighter fluid tends to against the gravitational force. In the second region, bubble velocity is relatively constant as compared to that of spike, which still accelerates downwards. On the center of geometry, the velocity of higher fluid will move downward due to the gravitational force. Because of existence of velocity difference, like the Bernoulli principle, the higher-pressure fluid will penetrate into the lower-pressure fluid to form a roll-up mushroom-shaped. The early roll-up of spike is formed at $T = 2$. This roll-up formation delays the bubble and spike

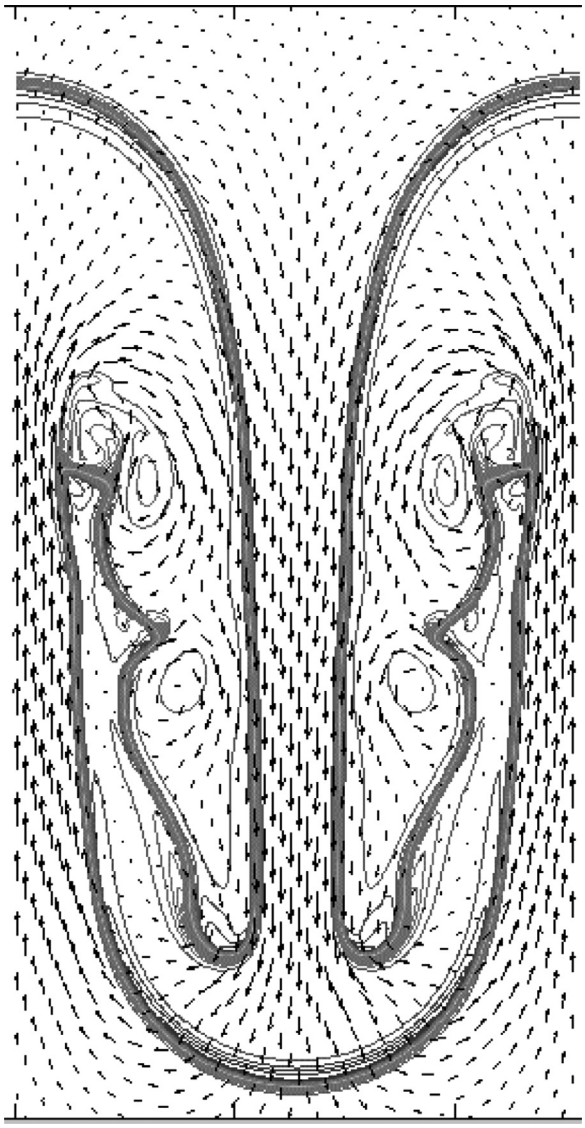

**Fig. 17.** Velocity field at the emerging of secondary fluid roll up.

movements. The formation of fluid roll up in spike is found in third region. The spike roll-up mechanism is initially formed as a result of fluids shear force interaction. The form of spikes vortex exhibits secondary instability of Kelvin-Helmholtz instability (KHI) emerged. The KHI causes fluids to roll-up, and forms other vortexes, which initiates fluid mixing phase. The second fluid roll-up appears at $T = 3.2$ and the velocity field is shown in Fig. 17. The formation of the second vortex yields the spike to re-accelerate, and then increases the bubble velocity. The re-acceleration of the spike pushes heavy fluid downward and gives additional force to the buoyancy force. Meanwhile, fluid roll-up formation pulls fluid within the fluid vortex, hence the bubble velocity is delayed. As the fluid roll-up mechanism is completed, bubble velocity will increase as shown at $T > 3.2$. The fourth region involves spike instability which is shown $T > 3.2$. The spike instability region is right before the fluid mixing stage. Both spikes and bubbles will be re-accelerated within the spike instability region. In this study, the bubble position will exponentially rise to obey the linear stability theory as reported in Ref. [2]. Sharp [15] identified that, when the fluid roll-up occurred as an exhibition of KHI, fluid vortex leads the fluid to be separated in the form of a bubble which stated as liquid breakup phenomenon. In this study, the liquid break-up can be successfully simulated as shown in Fig. 18.

The results are shown in Figs. 19 and 20 for early and late-stage instability, respectively. As mentioned above, in the early stage, the fluid roll-up as a result of KHI is formed, and the bubble rises. When the spike reaches the bottom, the turbulent mixing occurs as shown in Fig. 20(a) at $T > 8$. The denser fluid will directly move downward as the lighter fluid arises. The remaining lighter fluid is trapped inside the heavier fluid region and the bubble will be formed due to the

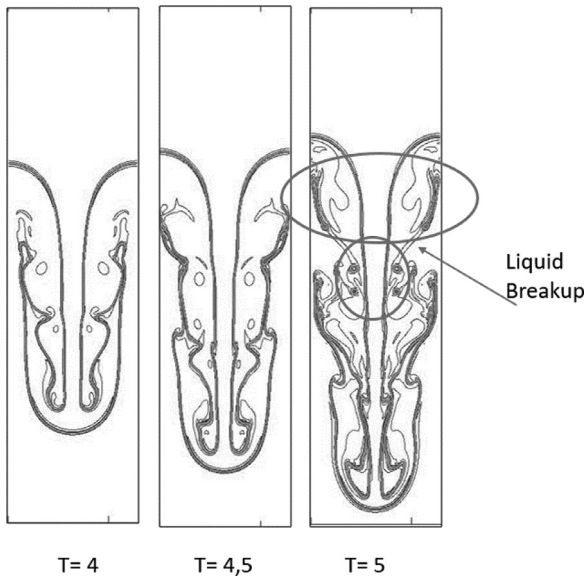


**Fig. 18.** Appearance of liquid break-up during KHI formation.

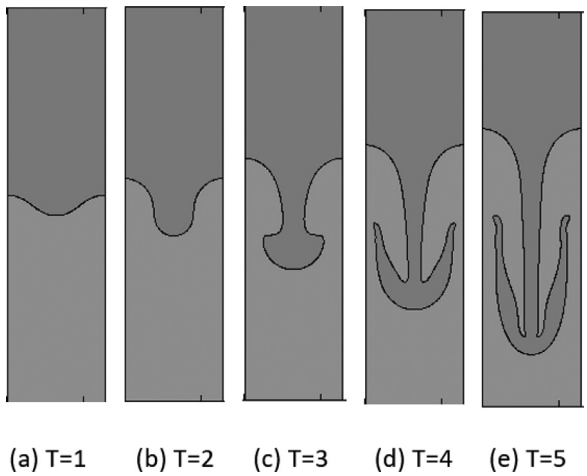


**Fig. 19.** Early stage of RTI simuation.

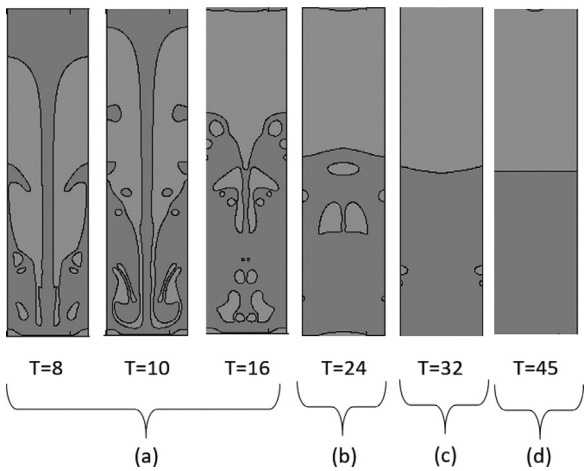


**Fig. 20.** Late stage of RTI simulation result.

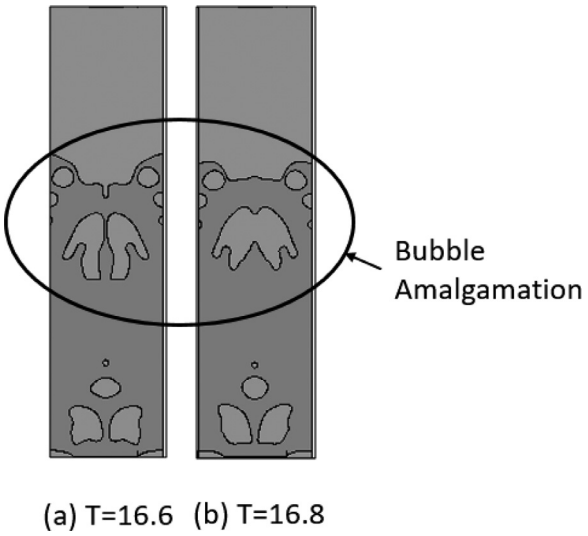


**Fig. 21.** The formation of bubble amalgamation.

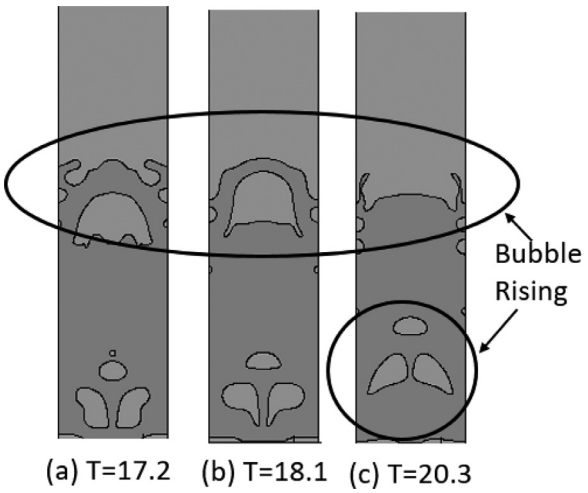


**Fig. 22.** Bubble rising at certain time.

emergence of surface tension force. The buoyancy force induces bubble rising as shown in Fig. 20(b). The interface of fluids experiences oscillation after the turbulent mixing condition completed, when the fluids have fully exchanged between each other (Fig. 20(c)). Furthermore, the gravitational force is not strong enough to make the lighter fluid to go through the dense fluid. The fluid interface oscillation will gradually decrease as time goes by. As shown in Fig. 20(d), the fluid reaches the equilibrium state, whereby the lighter fluid is situated above the heavier fluid.

The investigation of bubble amalgamation and bubble rise is reported in Fig. 21. At Fig. 21(a), two bubbles are formed and merged at $T = 16.8$ (Fig. 21(b)). Due to the similar value of both fluids surface tension, the bubble will merge between each other. Several small bubbles are then merged into a bigger bubble as a result of buoyancy force. This phenomenon was also reported by Ref. [47]. This result proves that the current LBM model is able to accurately simulate the bubble coalescence phenomenon. In Figs. 22(a) and (b), the bubble rise is observed at $T = 17.2$ - 18.1 right after the bubble coalescence. The subsequent bubble rise appears at $T = 20.3$ as shown in Fig. 22(c). The aforementioned facts indicate that the current LBM model can precisely simulate the bubble rise phenomenon.

## 4. Conclusion

A numerical study of the phenomena during RTI was conducted through the use of a Lattice-Boltzmann method. The method is proposed to analyze the turbulent mixing phenomena in liquid-liquid two-phase flow. The analyses performed in the present paper are able to accurately investigate a complete behavior of fluids interaction including conditions when instability occurs as well as the phenomena during the equilibrium state. The remarkable results are summarized as follows:

Good agreements are obtained when validating the results of current RTI simulation with those of experimental study and other numerical analyses. Convergence test is performed to obtain the optimum value of lattices. It is concluded that the total *MAPE* value of each numerical benchmark is less than 10% whereas for experimental comparison is obtained by 19.03%.

This study concludes that instability rate, expressed as traveled-distance of spikes and bubbles, is greatly affected by $A_t$. The decrease of $A_t$ and *Re* will delay the RTI development stages. For higher $A_t$, lighter fluid is quickly upwards due to the higher buoyancy force and vice versa. Meanwhile, *Re* is expressed to fluid's ability to be deformed. For higher *Re*, physical phenomena such as linear growth, fluid-roll up, fluid break-up, unstable vortices, and secondary instability are observed. Furthermore, both *Re* and $A_t$will affect the duration of the equilibrium state. The higher *Re* influences fluid to be more deformable and increase the duration of turbulent mixing and oscillation phase. In addition, the increase of $A_t$will reduce the turbulent mixing and surface oscillation phase due to the higher buoyancy force. In short, either increasing $A_t$ or reducing *Re* will accelerate the equilibrium state.

The analysis performed herein is able to completely simulate the behavior of fluids interaction including the secondary instability, i.e. KHI. In this regard, the simulation results can be separated into four regimes whereby KHI is shown in the third regime. The schematics of physical representation of fluids interaction in each regime were presented. Particularly, for KHI regime, the fluid roll-up formation emerges. This formation plays an important role in the reduction of the rate of instability. The knowledge of liquid-liquid instability is essential in the design consideration and operation safety of separators. In this study, we suggest that viscosity and density ratio of fluids are highly influential parameters and have significant effects in surge and residence time.

## Acknowledgement

This research is a part of postgraduate program supported by Indonesia Endowment Fund for Education (LPDP), Ministry of Finance, Republic of Indonesia. The authors would like to gratefully acknowledge for the fruitful discussion with Dr. Pranowo of Atma Jaya University, Dr. Eko Prasetya Budiana of Sebelas Maret University and Prof. Haibo Huang of University of Science and Technology of China for providing the information about the LBM. We also would like to express our appreciation to Center for Energy Studies for the research collaboration.

## References

[1] M. Deendarlianto, A. Andrianto, O. Widyaparaga, Khasani Dinaryanto, Indarto, CFD Studies on the gas-liquid plug two-phase flow in a horizontal pipe, J. Pet. Sci. Eng. 147 (2) (2016) 779–787.
[2] G. Yadigaroglu, S. Banerjee, G.F. Hewitt, Introduction to Multiphase Flow: Basic concepts, Applications and Modelling, Springer International Publishing, 2018.
[3] M.J.H. Simmons, E. Komonibo, B.J. Azzopardi, And D.R. Dick, "Residence Time Distributions And Flow Behaviour Within Primary Crude Oil–Water Separators Treating Well-Head Fluids," Vol. 82, No. October, pp. 1383–1390, 2004.
[4] Q. Zeng, Z. Wang, X. Wang, Y. Zhao, X. Guo, A novel oil – water separator design and its performance prediction, J. Pet. Sci. Eng. 145 (2016) 83–94.
[5] C.J. Backi, D. Krishnamoorthy, S. Skogestad, Slug handling on predictive gravity predictive gravity control for a gravity, IFAC-PapersOnLine 51 (8) (2018) 120–125.
[6] M. Mostafaiyan, M. Reza, A. Emami, M. Farahani, Application of evolutionary computational approach in design of horizontal three-phase gravity separators, J. Pet. Sci. Eng. 119 (2014) 28–35.
[7] T. Das, C.J. Backi, J. Jäschke, A model for subsea oil-water gravity separator to estimate unmeasured disturbances, Computer Aided Chemical Engineering 40 (2017) 1489–1494.
[8] T.T. Le, S.C. Ngo, Y.I. Lim, C.K. Park, B.D. Lee, B.G. Kim, D.H. Lim, Three-phase Eulerian computational fluid dynamics of air–water–oil separator under off-shore operation, J. Pet. Sci. Eng. 171 (April) (2018) 731–747.
[9] S. Shi-ying, X. Jing-yu, S. Huan-qiang, Z. Jian, L. Dong-hui, W. Ying-xiang, Experimental study of a vane-type pipe separator for oil – water separation, Chem. Eng. Res. Des. 90 (10) (2012) 1652–1659.
[10] B. Wiencke, Fundamental principles for sizing and design of gravity separators for industrial refrigeration, Int. J. Refrig. 34 (8) (2011) 2092–2108.
[11] A. Subramani, N. Christian, K. Lassen, J. Michael, J. Lund, S. Sasic, Segregation phenomena in gravity separators : a combined numerical and experimental study, Powder Technol 301 (2016) 679–693.
[12] J.W. Lord Rayleigh, Investigation of the Character of the Equilibrium of an Incompressible Heavy Fluid of Variable Density, Proc. London Math. Soc. 14 (39) (1883) 170–177.
[13] S.G. Taylor, The Instability of Liquid Surfaces when Accelerated in a Direction Perpendicular to their Planes. I, Proc. R. Soc. A Math. Phys. Eng. Sci. 202 (1068) (1950) 81–96.
[14] S. Chandrasekhar, Hydrodynamic and Hydromagnetic Stability, Oxford University Press, 1961.
[15] D.H. Sharp, An overview of Rayleigh-Taylor instability, Phys. D Nonlinear Phenom. 12 (1–3) (1984) 3–18.
[16] J. Glimm, J.W. Grove, X.L. Li, W. Oh, D.H. Sharp, A Critical Analysis of Rayleigh-Taylor Growth Rates, J. Comput. Phys. 169 (2) (2001) 652–677.
[17] X. He, S. Chen, R. Zhang, A Lattice Boltzmann Scheme for Incompressible Multiphase Flow and Its Application in Simulation of Rayleigh-Taylor Instability, J. Comput. Phys. 152 (2) (1999) 642–663.
[18] H. Liang, B.C. Shi, Z.H. Chai, An efficient phase-field-based multiple-relaxation-time lattice Boltzmann model for three-dimensional multiphase flows, Comput. Math. with Appl. 73 (7) (2017) 1524–1538.
[19] B.J. Daly, Numerical study of two fluid Rayleigh-Taylor instability, Phys. Fluids 10 (2) (1967) 297–307.
[20] H.G. Lee, J. Kim, Numerical simulation of the three-dimensional Rayleigh-Taylor instability, Comput. Math. with Appl. 66 (8) (2013) 1466–1474.
[21] H.G. Lee, K. Kim, J. Kim, On the long time simulation of the Rayleigh-Taylor instability, Int. J. Numer. Methods Eng. 85 (13) (Apr. 2011) 1633–1647.
[22] J.T. Waddell, C.E. Niederhaus, J.W. Jacobs, Experimental study of Rayleigh-Taylor instability: low atwood number liquid systems with single-mode perturbations, Phys. Fluids 13 (5) (2001) 1263–1273.
[23] D.J. Lewis, The instability of liquid surfaces when accelerated in a direction perpendicular to their planes. II, Proceedings of The Royal Society A 202 (December) (1949).
[24] J.P. Wilkinson, J.W. Jacobs, Experimental study of the single-mode three-dimensional Rayleigh-Taylor instability, Phys. Fluids 19 (12) (2007).
[25] A. Shimony, G. Malamud, D. Shvarts, Density Ratio and Entrainment Effects on Asymptotic Rayleigh–Taylor Instability, J. Fluids Eng. 140 (5) (2017) 050906.

[26] G. Dimonte, M. Schneider, Density ratio dependence of Rayleigh-Taylor mixing for sustained and impulsive acceleration histories, Phys. Fluids 12 (2) (2000) 304–321.
[27] M.R.E. Nasution, N. Watanabe, A. Kondo, Numerical study on thermal buckling of CFRP – Al honeycomb sandwich composites based on homogenization – localization analysis, Compos. Struct. 132 (2015) 709–719.
[28] H. Liang, Q.X. Li, B.C. Shi, Z.H. Chai, Lattice Boltzmann simulation of three-dimensional Rayleigh-Taylor instability, Phys. Rev. E 93 (3) (2016) 1–11.
[29] J.L. Guermond, L. Quartapelle, A Projection FEM for Variable Density Incompressible Flows, J. Comput. Phys. 165 (1) (2000) 167–188.
[30] E.P. Budiana, Pranowo, Indarto, Deendarlianto, Meshless numerical model based on radial basis function (RBF) method to simulate the Rayleigh–Taylor instability (RTI), Comput. Fluids (2020) 104472.
[31] G. Tryggvason, Numerical simulations of the Rayleigh-Taylor instability, J. Comput. Phys. 75 (2) (Apr. 1988) 253–282.
[32] A.A. Mohammed, Lattice Boltzmann method: Fundamentals and Engineering Applications With Computer Codes, Springer, 2011.
[33] T. Kruger, H. Kusumaatmaja, A. Kuzmin, O. Shardt, G. Silva, E.M. Viggen, The Lattice Boltzmann Method: Principles and Practice, Springer, 2017.
[34] Q. Li, K.H. Luo, Q.J. Kang, Y.L. He, Q. Chen, Q. Liu, Lattice Boltzmann methods for multiphase flow and phase-change heat transfer, Prog. Energy Combust. Sci. 52 (2016) 62–105.
[35] H. Huang, L. Wang, X.Y. Lu, Evaluation of three lattice Boltzmann models for multiphase flows in porous media, Comput. Math. with Appl. 61 (12) (2011) 3606–3617.
[36] L. Chen, Q. Kang, Y. Mu, Y. He, W. Tao, A critical review of the pseudopotential multiphase lattice Boltzmann model: methods and applications, Int. J. Heat Mass Transf. 76 (2014) 210–236.
[37] A.K. Gunstensen, D.H. Rothman, S.S. Zaleski, G. Zanetti, Lattice Boltzmann model of immiscible fluids, Phys. Rev. A 43 (8) (1991) 4320–4327.
[38] M.R. Swift, E. Orlandini, W.R. Osborn, J.M. Yeomans, Lattice Boltzmann simulations of liquid-gas and binary fluid systems, Phys. Rev. E - Stat. Physics, Plasmas, Fluids, Relat. Interdiscip. Top. 54 (5) (1996) 5041–5052.
[39] L. Chen, Q. Kang, Y. Mu, Y.L. He, W.Q. Tao, A critical review of the pseudopotential multiphase lattice Boltzmann model: methods and applications, Int. J. Heat Mass Transf. 76 (2014) 210–236.
[40] X. Shan, H. Chen, Lattice Boltzmann model for simulating flows with multiple phases and components, Phys. Rev. E 47 (3) (1993) 1815–1819.
[41] R. Zhang, X. He, S. Chen, Interface and surface tension in incompressible lattice Boltzmann multiphase model, Comput. Phys. Commun. 129 (1) (2000) 121–130.
[42] H. Huang, M. Sukop, X.Y. Lu, Lattice Boltzmann Simulations of Multiphase Flows, Wiley, 2013.
[43] J. Chao, R. Mei, R. Singh, W. Shyy, A filter-based, mass-conserving lattice Boltzmann method for immiscible multiphase flows, Int. J. Numer. Methods Fluids 66 (5) (Jun. 2011) 622–647.
[44] A. Fakhari, T. Mitchell, C. Leonardi, D. Bolster, Improved locality of the phase-field lattice-Boltzmann model for immiscible fluids at high density ratios, Physical Review E 96 (2017) 1–14.
[45] Y.Q. Zu, S. He, Phase-field-based lattice Boltzmann model for incompressible binary fluid systems with density and viscosity contrasts, Phys. Rev. E - Stat. Nonlinear, Soft Matter Phys. 87 (4) (2013) 1–23.
[46] F. Ren, B. Song, M.C. Sukop, H. Hu, Improved lattice Boltzmann modeling of binary flow based on the conservative Allen-Cahn equation, Phys. Rev. E 94 (2) (2016) 1–12.
[47] L. Amaya-bower, T. Lee, Computers & Fluids Single bubble rising dynamics for moderate Reynolds number using Lattice Boltzmann Method, Comput. Fluids 39 (7) (2010) 1191–1207.
[48] K.A. Yuana, B. Jalaali, E.P. Budiana, A. Pranowo, Lattice Boltzmann simulation of the Rayleigh–Taylor Instability (RTI) during the mixing of the immiscible fluids, European Journal of Mechanics - B/Fluids 85 (2021) 276–288.
[49] B. Jalaali, Pranowo, The lattice Boltzmann meshless simulation of multiphase interfacial-instability, AIP Conf. Proc. 2248 (2020) 040007.
[50] M. Geier, A. Fakhari, T. Lee, Conservative phase-field lattice Boltzmann model for interface tracking equation, Physical Review E 91 (2015).
[51] E. Castillo, J. Baiges, R. Codina, Approximation of the two-fluid flow problem for viscoelastic fluids using the level set method and pressure enriched finite element shape functions, J. Nonnewton. Fluid Mech. 225 (3) (2015) 37–53.
[52] Xuejuan Li, Ji-Huan He, Variational multi-scale finite element method for the two-phase flow of polymer melt filling process, Int. J. Num. Method Heat & Fluid Flow 30 (3) (2020) 1407–1426.